Preprints (www.preprints.org) | NOT PEER-REVIEWED | Posted: 29 September 2018 doi:10.20944/preprints201809.0583.v1

Peer-reviewed version available at Catalysts 2018, 8, 625; doi:10.3390/catal8120625

Article

Photocatalytic Degradation of Estriol using Iron-doped TiO_2 under High and Low UV-irradiation

Irwing M. Ramírez-Sánchez [1], Erick R. Bandala [2,3,*]

[1] Department of Civil, Architectural and Environmental Engineering, The University of Texas at Austin, Austin, Tx 78712, USA; irwingmoises@gmail.com (I.M.R);
[2] Desert Research Institute (DRI). 755 E. Flamingo Road. Las Vegas, 89119-7363 Nevada, USA
[3] Graduate Program Hydrologic Sciences. University of Nevada, Reno. Reno, NV 89557, USA
* Correspondence: erick.bandala@dri.edu (E.R.B)

Abstract: Iron Doped TiO_2 nanoparticles (Fe-TiO_2) were synthesized and photocatalitically investigated under high and low fluence values of UV-radiation. The Fe-TiO_2 physical characterization was performed using X-ray Powder Diffraction (XRD), Brunauer-Emmett-Teller (BET) surface area analysis, Transmission Electron Microscope (TEM), Scanning Electron Microscope (SEM), Diffuse Reflectance Spectroscopy (DRS), and X-Ray Photoelectron Spectroscopy (XPS) technique. The XPS evidenced that ferric ion (Fe^{3+}) was in the lattice of TiO_2 and co-dopants no intentionally added were also present due to the precursors of the synthetic method. The Fe^{3+} concentration played a key role in the photocatalytic generation of hydroxyl radical (•OH) and estriol (E3) degradation. Fe-TiO_2 materials accomplished E3 degradation, and it was found that the catalyst with 0.3 at. % content of Fe (0.3 Fe-TiO_2) enhanced the photocatalytic activity under low UV-irradiation compared with no intentionally Fe-added TiO_2 (zero-iron TiO_2) and Aeroxide® TiO_2 P25. Furthermore, the enhanced photocatalytic activity of 0.3 Fe-TiO_2 under low UV-irradiation may have applications when radiation intensity must be controlled, as in medical applications, or when strong UV absorbing species are present in water.

Keywords: Iron-doped TiO_2, photocatalytic activity, low UV-irradiation, hydroxyl radical, estriol.

1. Introduction

In recent years, society and scientific community have become aware of Emerging Contaminants (ECs, also called Contaminants of Emerging Concern). ECs are chemicals that are not currently covered by existing local or international water quality regulations threating the environment, human health, and water safety [1]. ECs include chemical species such as algae toxins, illegal drugs, industrial compounds, flame retardant, food additives, nanoparticles, pharmaceuticals (human and vet), personal care products, pesticides, biocides, steroid, synthetic and natural hormones, and surfactants [2].

Natural estrogens (e.g., estrone (E1), 17β-estradiol (E2) and estriol (E3)) are ECs capable of persisting and bioaccumulating in the environment giving rise to endocrine disruption on human and wildlife (vertebrates [3–5] and invertebrates [6,7]). Natural attenuation, drinking water purification or conventional municipal wastewater treatment processes are either only partially or incapable of removing estrogens [8]. As result, water treatment techniques have been developed to manage, reduce, degrade, and mineralize low-concentrated ECs (including natural estrogen) in drinking and wastewater [9]. Advanced Oxidation Process (AOPs) have been reported as a promising technique and, among AOPs, photocatalytic processes using titanium dioxide (TiO_2) has been identified as one of the most effective methods to degrade estrogens in water [10]. Several

© 2018 by the author(s). Distributed under a Creative Commons CC BY license.

Preprints (www.preprints.org) | NOT PEER-REVIEWED | Posted: 29 September 2018 doi:10.20944/preprints201809.0583.v1

Peer-reviewed version available at Catalysts 2018, 8, 625; doi:10.3390/catal8120625

reports recognized TiO_2 to degrade estrogens, avoiding increases in estrogenic activity in water [11,12] and able of partially or completely mineralize estrogens [11,13].

TiO_2 is the most commonly used photocatalyst due to its reasonable optical and electronic properties, good photocatalytic activity, insolubility in water, chemical and photochemical stability, non-toxicity, low cost and high efficiency in pollutant mineralization [14–17]. However, the band gap energy (E_g) of TiO_2, frequently reported of 3.2 eV [18], restrains the photocatalytic activation to energy sources with a portion of spectrum emission below 387.5 nm [19] (Figure 1). Consequently, reduction of the photon energy needed for TiO_2 photoactivation has drawn the attention of the scientific community up to now. Different techniques have been tested to control or modify the surface properties or internal structure of TiO_2; doping is one of them. Doping introduces a foreign element into TiO_2 to cause an impurity state into the band gap. The doping materials most frequently used have been transition-metal cations (*e.g.*, Cr, V, Fe, Ni) at Ti sites, and anions (*e.g.*, N, S, C) at O sites [20]. Among anion- and cation-dopants, ferric ion (Fe^{3+}) is one of the most often employed because Fe^{3+} ionic radius (0.69 A) is similar to Ti^{4+} (0.745 A), so Fe^{3+} can be easily incorporated into the TiO_2 crystal lattice [21].

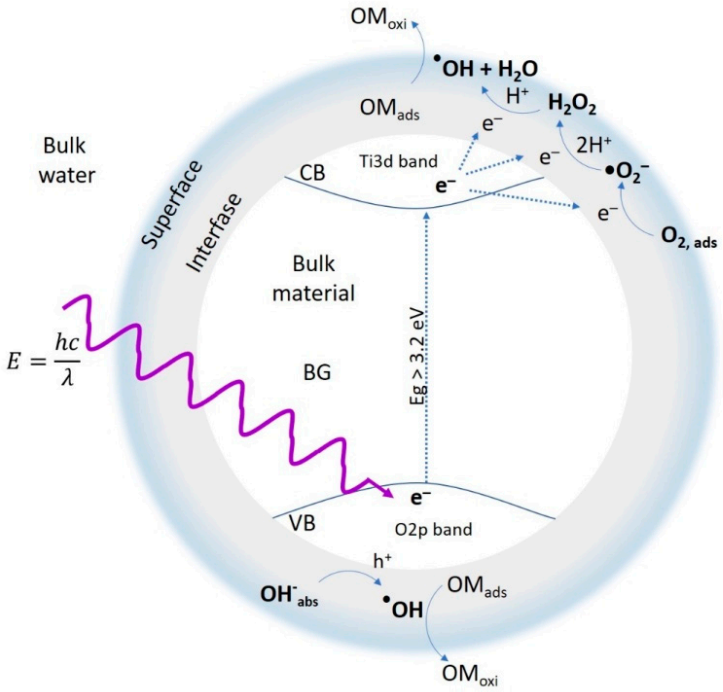

Figure 1. Photocatalytic TiO_2 mechanism for •OH generation. According to Density Functional Theory (DFT) computations, the valence band (VB) and conduction band (CB) of pure TiO_2 are mainly composed of O 2p orbitals and Ti 3d orbitals, respectively. Hence, the Fermi level (EF) is located in the middle of the band gap (BG), indicating that VB is full filled while CB is empty [22]. When using photons with energy higher than 3.2 eV, photoexcitation of the semiconductor promotes electrons from VB to CB creating a charge vacancy (hole) in the VB. The hole in the VB can react with hydroxide ion to form hydroxyl radical (•OH) or can also be filled by donor absorbed organic molecule. Photogenerated electrons in the CB can be transferred to acceptor of electrons and bring about •OH. Where E_g: Band gap energy; E: photon energy; OM_{ads}; adsorbed organic molecule; and OM_{oxi}: oxidized organic molecule.

In general, the effect of Fe on photocatalytic activity of doped TiO_2 rapidly raises with increasing Fe doping, then reaches a maximum value, and finally decreases with further increases of Fe content [22–34]. Even detrimental effects have been mentioned when comparing undoped Fe TiO_2 nanoparticles with high Fe-content TiO_2 [35,36], or agglomerated Fe-TiO_2 nanoparticles [37,38]. Although different theoretical and experimental studies have been developed about Fe-TiO_2, the trade-off between optimal doping ratio, and intensity of radiation is scarcely mentioned. In this work, Fe-TiO_2 nanoparticles were synthesized and studied to increase the understanding on the

Preprints (www.preprints.org) | NOT PEER-REVIEWED | Posted: 29 September 2018 doi:10.20944/preprints201809.0583.v1

Peer-reviewed version available at Catalysts 2018, 8, 625; doi:10.3390/catal8120625

relationship between doping ratio and radiation intensity for •OH generation and E3 degradation. Furthermore, Fe-TiO_2 photocatalyst has rarely been considered as a useful technique for the degradation of E3 [39]. Therefore, we investigated the photocatalytic degradation of E3 using Fe-TiO_2 under high and low UV-irradiation. We highlight the term low-UV irradiation to avoid misunderstanding with the term Visible-light photocatalytic processes because we did not intentionally use a cut-off UV-filters for experiments.

2. Results and Discussion

2.1. Characterization of Iron doped TiO_2

Figure 2 shows X-Ray Photoelectron Spectroscopy (XPS) general spectra of no intentionally Fe-added TiO_2 (zero-iron TiO_2) and Fe-TiO_2 materials. For the experimental condition used, no differences were seen showing that Fe did not affect the bonding structure between titanium and oxygen. For all samples, the main peaks were Ti2p and O1s with the proportion 1:2.2, in agreement with the atomic formula of TiO_2.

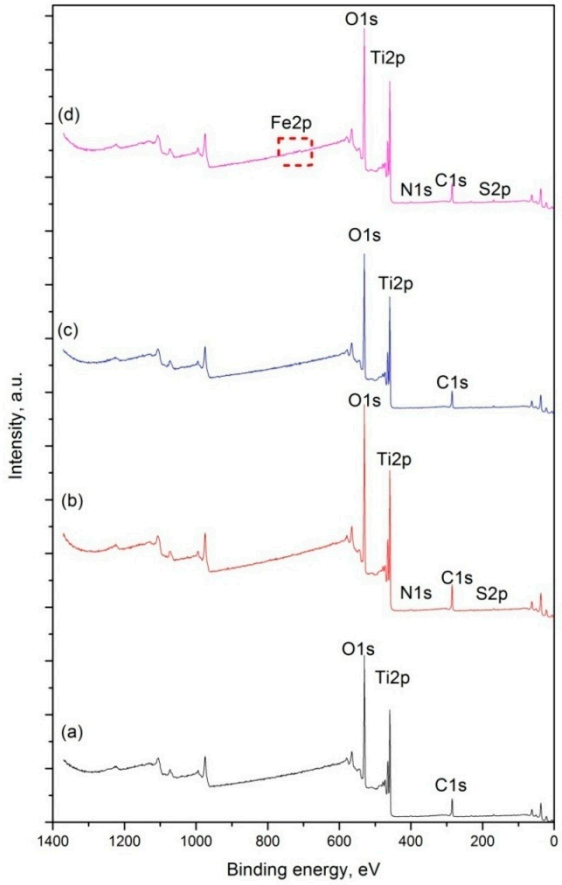

Figure 2. XPS general spectra for zero-iron TiO_2 (a), 0.3 Fe-TiO_2 (b), 0.6 Fe-TiO_2 (c), and 1.0 Fe-TiO_2 (d).

Also, XPS detected non-intentionally added elements (Table 1) as co-dopants of Fe-TiO_2 such as C, S, and N which were introduced in TiO_2 via precursors of the synthesis such as SDS and HNO_3.

Preprints (www.preprints.org) | NOT PEER-REVIEWED | Posted: 29 September 2018 doi:10.20944/preprints201809.0583.v1

Peer-reviewed version available at Catalysts 2018, 8, 625; doi:10.3390/catal8120625

Table 1. Surface elemental composition as determined XPS.

Material	Atomic % of elements (at. %)					
	Ti2p	O1s	C1s	Fe2p	S2p	N1s
Zero-iron TiO_2	24.4	52.9	21.3	0	1.4	-
0.3 Fe-TiO_2	23.8	51.1	22.9	0.3	1.1	0.8
0.6 Fe-TiO_2	23.9	53.1	22.5	0.6	-	-
1.0 Fe-TiO_2	23.5	52.5	20.6	1	1.5	0.9

High-resolution XPS spectra for the iron region (Figure 3) was studied only for 1.0 Fe-TiO_2 since no Fe2p signals were detected for zero-iron TiO_2, 0.3 Fe-TiO_2, or 0.6 Fe-TiO_2 (Figure 2) maybe because these Fe doping loads were below the XPS analysis detection limit. The deconvolution of high-resolution XPS spectra (Figure 3) was developed for peaks previously reported for Fe^{2+} and Fe^{3+} [40] using the software XPSpeak 4.1. The baseline used was Shirley subtracted before peak fitting. Gaussian–Lorentzian mix function was employed with a 40% factor. Charge compensation was set by the O1s peak charge with -0.58 eV. The correlation between the experimental signal with the theoretic model ($\Sigma\chi^2$) was 8.43×10^{-2}.

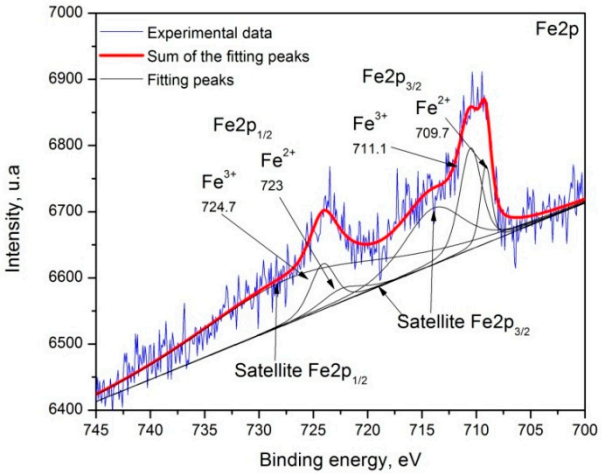

Figure 3. High-resolution XPS spectra for the iron region for 1.0 Fe-TiO_2.

According to the theoretical model, both Fe^{3+} and Fe^{2+} were present in the lattice of 1.0 Fe-TiO_2. Since Fe^{3+} ionic radius (0.69 A) is similar to Ti^{4+} (0.745 A), Fe^{3+} was incorporated into the lattice of TiO_2 to form Ti–O–Fe bonds [21]. Probably, XPS technique detected Fe^{2+} because the Fe^{3+} underwent reduction to Fe^{2+} during XPS measurement in vacuum [41].

E_g value obtained with the Kubelka-Monk method (Figure 4) for Aeroxide® TiO_2 P25 was 3.2 eV, consistent with earlier reported value [42]. In general, and respect to zero-iron TiO_2, E_g values for Fe-TiO_2 materials (Table 2) decreased as long as Fe content increased, so Fe content raised red-shift. Compared to Aeroxide® TiO_2 P25, red-shift were 0.22 eV, 0.24, 0.25, and 0.3 eV for Zero-Fe TiO_2, 0.3 Fe-TiO_2, 0.6 Fe-TiO_2, and 1.0 Fe-TiO_2 respectively. Shi *et al.* reported a red-shift of E_g value for Fe-TiO_2 of 0.25 eV (from 3.24 to 2.99 eV) [43]. Also based on density functional theory calculations, other works suggested the hybridized band with Ti 3d and Fe 3d reduces E_g about 0.3-0.5 eV [41], or 0.2 - 0.34 eV [44]. The red-shift of Fe TiO_2 was found in agreement with previously reported values respect to Aeroxide® TiO_2 P25, but less with respect to zero-iron TiO_2. So red-shift was given rise not only related to Fe content but also the synthesis method and co-doped Fe TiO_2.

Preprints (www.preprints.org) | NOT PEER-REVIEWED | Posted: 29 September 2018 doi:10.20944/preprints201809.0583.v1

Peer-reviewed version available at Catalysts 2018, 8, 625; doi:10.3390/catal8120625

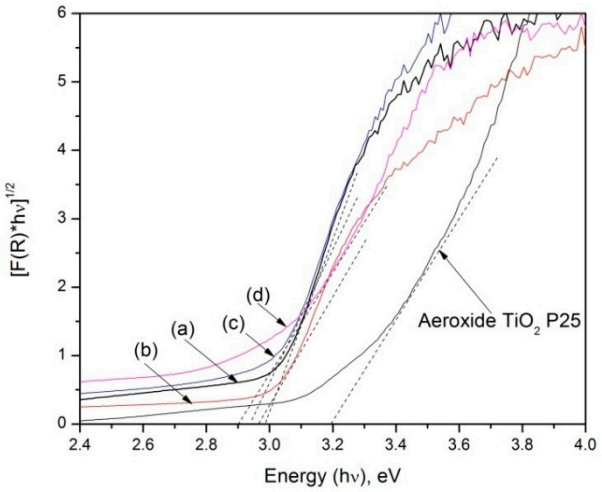

Figure 4. The Kubelka-Monk method for zero-iron TiO_2 (a), 0.3 Fe-TiO_2 (b), 0.6 Fe-TiO_2 (c), and 1.0 Fe-TiO_2 (d).

XRD patterns depicted in Figure 5 revealed zero-iron TiO_2 and Fe-TiO_2 materials had both anatase and rutile phases. No XRD Fe_2O_3 peaks (2θ = 33.0°, 35.4°, 40.7°, 43.4°, and 49.2) were observed, concluding that Fe^{3+} replaced Ti^{4+} in the TiO_2 crystal framework [45,46]. These results support the synthesis method allowed uniform distribution of Fe within TiO_2. The anatase: rutile phase ratio calculated by Spurr and Myers' method showed that zero-iron TiO_2 and Fe-TiO_2 materials were a mixtures of anatase and rutile phases (Table 2). The amount of anatase was less in Fe-TiO_2 materials than in Aeroxide® TiO_2 P25. The less proportion of anatase could lead to a reduction of photocatalytic activity because anatase phase has higher photocatalytic activity than rutile TiO_2 [47,48]. However, it is accepted that the optimal photocatalytic activity of TiO_2 is reached with mixture of anatase and rutile phases [49]. Moreover, an increase of anatase proportion in 0.3 Fe-TiO_2 and 0.6 Fe-TiO_2 compared with zero-iron TiO_2 could improve its photocatalytic activity. The anatase proportion increase was attributable to Fe doping disturbing the arrangements of TiO_2 phases [50] and the same trend has also been observed when synthesized using sol-gel [51], or co-precipitation method [29].

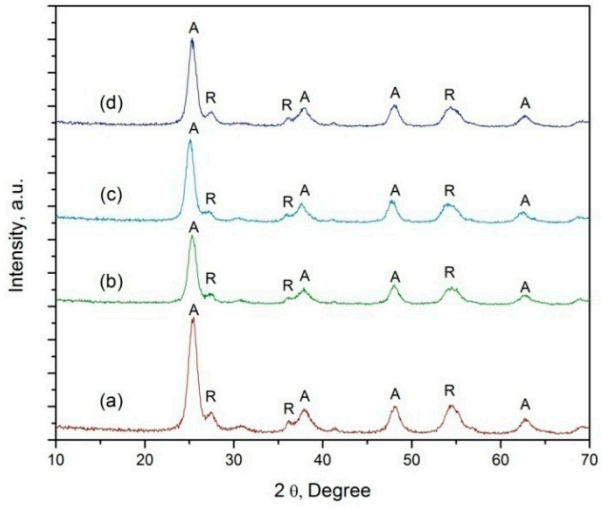

Figure 5. XRD patterns for zero-iron TiO_2 (a), 0.3 Fe-TiO_2 (b), 0.6 Fe-TiO_2 (c), and 1.0 Fe-TiO_2 (d)., where A- Anatase and R- Rutile phases.

Preprints (www.preprints.org) | NOT PEER-REVIEWED | Posted: 29 September 2018 doi:10.20944/preprints201809.0583.v1

Peer-reviewed version available at Catalysts 2018, 8, 625; doi:10.3390/catal8120625

Particle size affects the photocatalytic activity of TiO_2. Hence, the average particle size of Fe-TiO_2 materials obtained by Scherer´s formula was 6.9 nm which is less than the particle size of Aeroxide® TiO_2 P25 (Table 2), Fe-TiO_2 materials should increase the activity because of higher surface area and short distance for migration of photogenerated charge carriers (electron/hole (e^-/h^+)) form the bulk material to the surface. Further Brunauer-Emmett-Teller (BET) analysis confirmed that average surface area of Fe-TiO_2 materials was 77.9 $m^2\ g^{-1}$, higher than zero-iron TiO_2 and Aeroxide® TiO_2 P25.

BET isotherms (Figures 6) followed a type IV shape according to the Langmuir classification, associated with the characteristics of mesoporous material [52]. The observed hysteresis is probably due to gas cooperative adsorption or condensation inside the pores of material [53]. BET analysis showed pore sizes (Table 2) were in the mesoporous range (2- 50 nm, according to IUPAC classification) for zero-iron TiO_2, and 1.0 Fe-TiO_2, and microporous (0.2-2 nm, according to IUPAC classification) for 0.3 Fe-TiO_2, and 0.6 Fe-TiO_2. Mesoporous pore size is expected should facilitate mass transfer of reactants and products in the reaction system, so photocatalytic improvement based on this property could be expected in Aeroxide® TiO_2 P25 respect to zero-iron TiO_2 and Fe-TiO_2 materials [28].

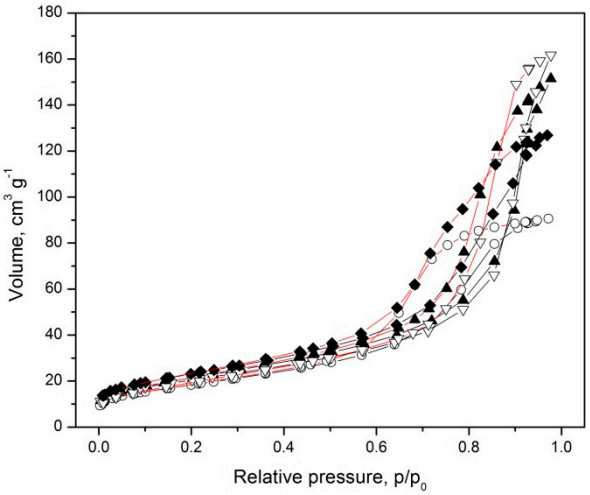

Figure 6. Brunauer-Emmett-Teller (BET) isotherms for ○ zero-iron TiO_2, ▲ 0.3 Fe-TiO_2 TiO_2, ▽0.6 Fe-TiO_2, and ◆ 1.0 Fe-TiO_2; where the black line is adsorption, and the red line is desorption.

Patra et al. [46] developed a similar nanoparticles synthesis procedure which generated surface area values in the 126 and 385 $m^2\ g^{-1}$ range and mesoporous size distribution values ranging 3.1 and 3.4 nm. Particles obtained in our work were different probably because mild thermal treatment applied and use of SDS critical micelle concentration as template.

Figure 7 shows SEM images of agglomerated and assembled nanoparticles of zero-iron TiO_2. The different Fe amounts into the TiO_2 lattice neither changed morphology nor particle size of zero-iron TiO_2. Although the average pore size allows an increase of superficial area, the agglomeration could lead to lower photocatalytic activity.

Preprints (www.preprints.org) | NOT PEER-REVIEWED | Posted: 29 September 2018 doi:10.20944/preprints201809.0583.v1

Peer-reviewed version available at Catalysts 2018, 8, 625; doi:10.3390/catal8120625

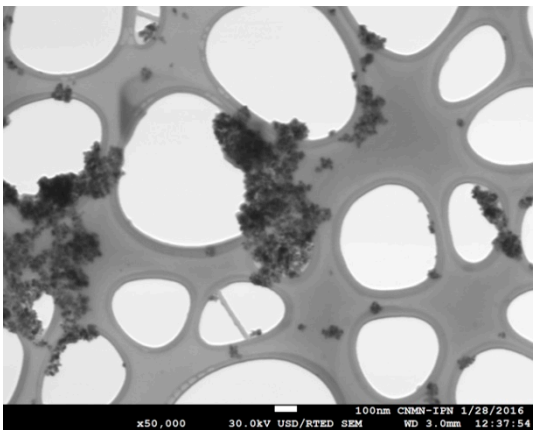

Figure 7. SEM image of zero-iron TiO_2 after mechanical grinding and sonication.

Transmission electron microscopy (TEM) images confirmed nanoparticle clusters and particle size of zero-iron TiO_2 (Figure 8b) and 0.3 Fe-TiO_2 (Figure 8a) between 5 and 10 nm (between 1.2 and 9.4 nm according to Scherer´s formula). The lattice fringe spacing was 0.35 nm as shown in Figure 8b, which was consistent with the d-spacing (101) of anatase [54]. The lattice fingers of the nanoparticles showed that Fe-TiO_2 materials were highly crystallized.

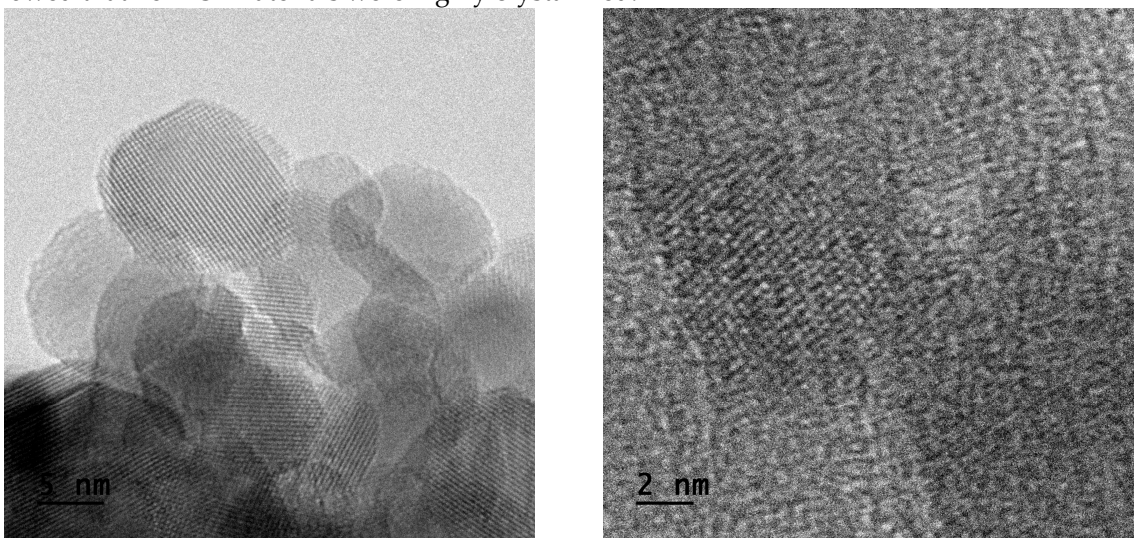

(a) (b)

Figure 8. Transmission electron microscopy (TEM) image of 0.3 Fe-TiO_2 (a) and zero-iron TiO_2 (b).

2.2. Characterization of Irradiation Source

In Figure 9, the emission spectra of irradiation sources used in this report are showed. Using main peaks reported for a fluorescent lamp (Figure 9a), the calibration of the spectrometer generated R^2 value equal to 0.999. The emission spectrum of GE F15T8 BLB lamp (Figure 9b) was a band from 356 to 410 nm. Meanwhile, the emission spectrum of the GE F15T8 D lamp (Figure 9c) was continuous broadband from 380 to 750 nm.

Preprints (www.preprints.org) | NOT PEER-REVIEWED | Posted: 29 September 2018 doi:10.20944/preprints201809.0583.v1

Peer-reviewed version available at Catalysts 2018, 8, 625; doi:10.3390/catal8120625

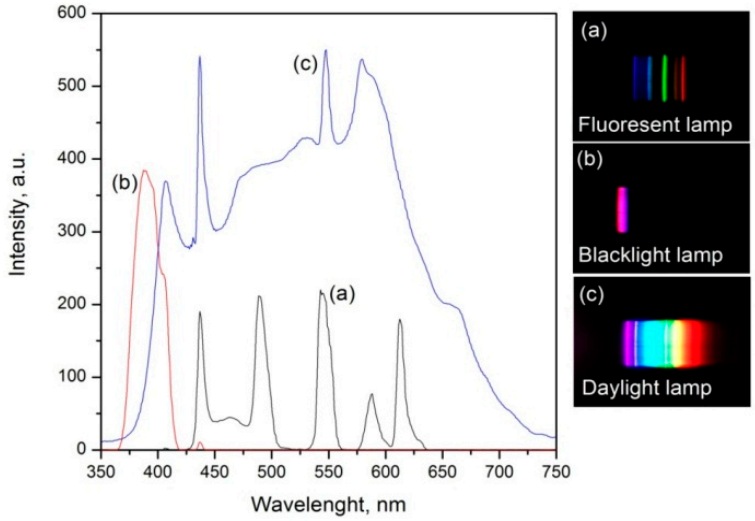

Figure 9. Emission spectrum and intensity graph of the irradiation source of Tecnolite fluorescent lamp (a), GE F15T8 BLB lamp (b), and GE F15T8 D lamp (c).

Because E_g of Aeroxide® TiO_2 P25 is 3.2 eV (387.5 nm), both GE F15T8 BLB and GE F15T8 D lamp emitted photons that could photo activate Aeroxide® TiO_2 P25. However, the proportion of emission spectrum than Aeroxide® TiO_2 P25 can use for photocatalytic activity was different, so the radiative intensity. An approximation of the amount of radiative intensity used to photocatalytic activity was obtained with the area under the curve-spectrum below E_g value. Consequently, Aeroxide® TiO_2 P25 could take advantage of 36.4 % of the emission spectrum of GE F15T8 BLB lamp, and 0.8 % of the emission spectrum of GE F15T8 D lamp. Thus, GE F15T8 BLB lamp and GE F15T8 D lamp were named as high and low UV-irradiation source respectively. Similarly, the amount of radiative spectrum used by zero-iron TiO_2 and Fe-TiO_2 materials is mention in Table 2.

Table 2. Structural and optical properties of zero-iron TiO_2, and Fe-TiO_2.

Material	E_g		Anatase: Rutile	Particle size	Surface area	Pore size	High UV	Low UV
	eV	nm	%	nm	$m^2\ g^{-1}$	nm	%	%
Aeroxide® TiO_2 P25*	3.2	387.5	80:20	21	50 ± 15	17.5	36.4	0.8
Zero-iron TiO_2	2.98	416.1	73.1:26.9	6.6	66.5	8.4	99.26	7.64
0.3 Fe-TiO_2	2.96	418.9	77.9:21.1	6.9	77.6	1.2	99.40	8.21
0.6 Fe-TiO_2	2.95	420.3	78.8:21.2	7.1	73.0	1.4	99.42	8.77
1.0 Fe-TiO_2	2.90	427.6	76.3:23.7	6.9	83.1	9.4	99.43	10.63

[*] According to the manufacturer

Based on morphological and crystalline structure analysis, the favorable characteristic which could enhance photocatalytic activity of TiO_2 are: effective insertion of Fe^{3+} ion into the TiO_2 lattice, red-shift (2.90-2.96 eV), nanoparticle size (6.9-7.1 nm), specific surface area (73.0 -83.1 nm), pore size (1.2-9.4 nm), and radiation absorbance below equivalent E_g wavelength (8.21 - 10.63% of daylight lamp spectrum). Its main disadvantageous characteristics are expected to be high particle agglomeration and lower anatase phase compared to zero-iron TiO_2. Further, photocatalytic activity is very sensitive to crystalline array, particle size, and shape; differences in the density of hydroxyl groups on the particle surface and the number of water molecules hydrating the surface; surface area and surface charge; differences in the number and nature of trap sites; dopant concentration, localization and chemical state of the dopant ions; intensity radiation; particle aggregation, and superficial charge; or scavenger species in media [36,55]. In consequence, material characterization alone could not predict the photocatalytic activity [25]. Thus, in this research, we used the pNDA

Preprints (www.preprints.org) | NOT PEER-REVIEWED | Posted: 29 September 2018 doi:10.20944/preprints201809.0583.v1

Peer-reviewed version available at Catalysts 2018, 8, 625; doi:10.3390/catal8120625

probe and E3 to evaluate the photocatalytic activity by following •OH production which is one of the most significant reactive oxygen species (ROS) and E3 an endocrine disrupting chemical (EDC).

2.3. Hydroxyl Radical Generation under High and Low UV-irradiation

Generation of •OH was measured using pNDA, a very well characterized •OH scavenger widely reported in the literature [48,56–59]. In brief, pNDA undergoes bleaching when reacting with •OH according to Eqs. (1) and (2) [60].

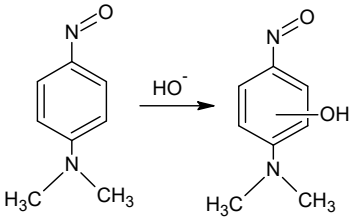

(1)

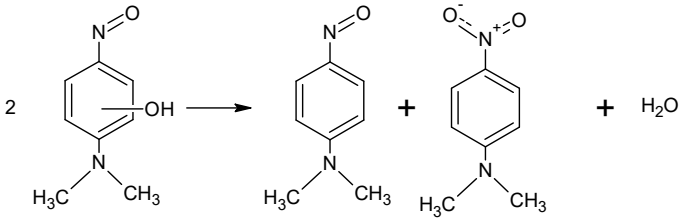

(2)

In this work, pNDA bleaching followed pseudo-first-order equation, so the apparent rate constant was calculated by $\ln(C/C_0)=k_1 t$, where C_0 is the initial concentration, C reaction concentration at given time, and k_1 pseudo-first order reaction rate constant. The slope of the plot after applying a linear fit represents the rate constant, k_1.

Because of 1:1 stoichiometry relationship between bleaching-pNDA and •OH-abducted as mentioned in Eqs. (1) and (2), •OH generation is a steady-state value ($[^{\bullet}OH]_{ss}$) equals the initial velocity (r_0, in Table 3) of pNDA-bleaching according to Eq. (3).

$$\left.\frac{[pNDA]}{dt}\right|_{t=0} = r_0 = [\,^{\bullet}OH]_{ss} \quad (3)$$

Table 3. •OH generation rate of zero-iron TiO_2 and Fe-TiO_2.

Catalyst	at. %	Load	High UV-irradiation			Low UV-irradiation		
			k_1	R^2	$r_{0,OH}$	k_1	R^2	$r_{0,OH}$
		mg L^{-1}	min^{-1}		μM•OH min^{-1}	min^{-1}		μM•OH min^{-1}
TiO_2 Aeroxide® P25	-	20	0.06	0.988	0.49	0.012	0.989	0.105
Zero-iron TiO_2	0	320	0.056	0.993	0.49	0.005	0.973	0.045
0.3 Fe-TiO_2	0.3	320	0.067	0.998	0.58	0.004	0.990	0.042
0.6 Fe-TiO_2	0.6	320	0.031	0.998	0.28	0.002	0.999	0.025
1.0 Fe-TiO_2	1	320	0.004	0.987	0.04	0.00002	0.891	0.0002

Because Fe-TiO_2 materials showed similar anatase: rutile phase ratio, particle size, and specific surface area, variation in r_0 is suggested due to the difference of Fe content within TiO_2. Generation of •OH radicals (r_0) were feasible using zero-iron TiO_2, Fe-TiO_2 materials and Aeroxide® TiO_2 P25 both under high (Figure 10a) and low UV-radiation (Figure 10b).

Preprints (www.preprints.org) | NOT PEER-REVIEWED | Posted: 29 September 2018 doi:10.20944/preprints201809.0583.v1

Peer-reviewed version available at Catalysts 2018, 8, 625; doi:10.3390/catal8120625

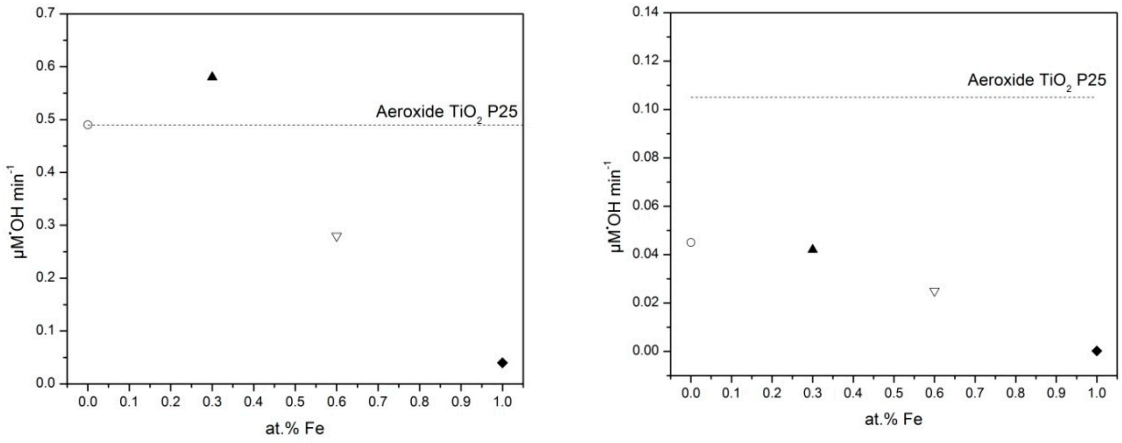

(a) (b)

Figure 10. •OH generation of zero-iron TiO_2 and Fe-TiO_2 under high UV-irradiation (a) and low UV-Irradiation (b); where ○ zero-iron TiO_2, ▲ 0.3 Fe-TiO_2 TiO_2, ▽0.6 Fe-TiO_2, and ◆ 1.0 Fe-TiO_2 at pH 6 ± 0.1, and 20 °C.

When high UV-irradiation was used, maximum r_0 was 0.58 $\mu M_{\bullet OH}$ min^{-1} for 0.3 Fe-TiO_2. Compared with zero-iron TiO_2 and Aeroxide® TiO_2 P25, the photocatalytic activity observed was higher and lower, respectively. The enhancement in photocatalytic activity compared to zero-iron TiO_2 could be rationalized by the extended lifetime values of the photogenerated charge carriers (electrons and holes) produced by Fe^{3+} ions playing a role as charge carriers trap at or near the particle surface, as proposed in Eqs. (4) to (7) [61].

$$Fe^{3+} + e_{cd}^{-} \rightarrow Fe^{2+} \quad \text{electron trap} \quad (4)$$

$$Fe^{2+} + Ti^{4+} \rightarrow Fe^{3+} + Ti^{3+} \quad \text{migration} \quad (5)$$

$$Fe^{3+} + h_{vb}^{+} \rightarrow Fe^{4+} \quad \text{hole trap} \quad (6)$$

$$Fe^{4+} + OH^{-} \rightarrow Fe^{3+} + {}^{\bullet}OH \quad \text{migration} \quad (7)$$

The mechanism suggested for •OH generation is that Fe^{3+} induces an impurity level into the lattice of TiO_2 below the CB acting like a shallow tramp for photogenerated electrons as depicted in Figure 11 [41].

Preprints (www.preprints.org) | NOT PEER-REVIEWED | Posted: 29 September 2018 doi:10.20944/preprints201809.0583.v1

Peer-reviewed version available at Catalysts 2018, 8, 625; doi:10.3390/catal8120625

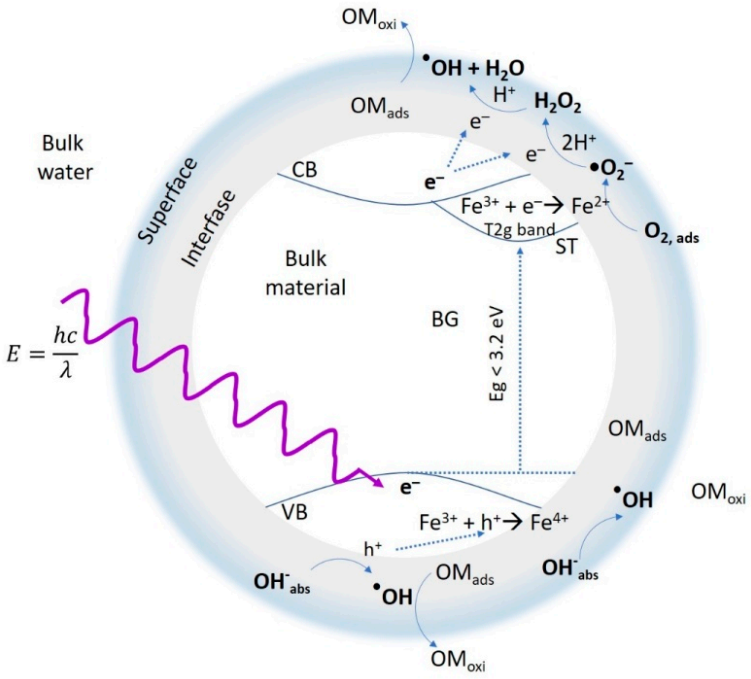

Figure 11. Photocatalytic mechanism of Fe-TiO_2 and •OH generation. When TiO_2 contains a Fe^{3+} ion, the Fe 3d orbitals split into two bands, one is a hybrid band (A2g), and one is midgap band (T2g) which induce a new localized BG state [22]. Thus, when TiO_2 absorb photons with energy less than 3.2 eV, photoexcitation of the semiconductor promotes an electron from the VB to the midgap band (T2g), also called shallow trap, creating a pair electron/hole. The hole in the valence band (VB) can react with hydroxide ions to form •OH, absorbed organic molecules or trap for Fe^{3+}. Also, photogenerated electrons in the midgap band (T2g) can be transferred to Fe^{3+} and later trapped photogenerated electron can transfer to acceptor of electrons and bring about •OH. E_g – band gap energy, E – photon energy, OM_{ads} - adsorbed organic molecule, OM_{oxi} - oxidized organic molecule.

Excessive Fe^{3+} doping was found unfavorable to the photocatalytic activity because the additional Fe^{3+} doping in the TiO_2 sample could act as recombination sites decreasing the photocatalytic efficiency [26]. The localization of the Fe^{3+} cations inside the TiO_2 lattice has been suggested inhibiting the extended lifetime of charge carries acting as electron-hole pair recombination center as proposed in Eqs. (8) to (11) [36].

$$Fe^{2+} + h_{vb}^{+} \rightarrow Fe^{3+} \quad \text{recombination} \quad (8)$$

$$Fe^{4+} + e_{cd}^{-} \rightarrow Fe^{3+} \quad \text{recombination} \quad (9)$$

$$Fe^{4+} + Fe^{2+} \rightarrow 2Fe^{3+} \quad \text{recombination} \quad (10)$$

$$Fe^{4+} + Ti^{3+} \rightarrow Fe^{3+} + Ti^{4+} \quad \text{recombination} \quad (11)$$

When low UV-irradiation conditions were used, the r_0 values for zero-iron TiO_2 and Fe-TiO_2 were lower than the value estimated for Aeroxide® TiO_2 P25. Compared with undoped TiO_2, the reduction in r_0 value observed for Fe-TiO_2 materials could be related to the increased recombination rate produced by the augmented Fe content. Also, pNDA adsorption of UV-visible radiation may act as a chemical filter, lowering the number of photons available to activate the photocatalyst. We noticed a strong radiation absorption by pNDA which overlapped with the E_g region of zero-iron TiO_2 and Fe-TiO_2 materials (see Table 2) and consider pNDA may not be a suitable probe for hydroxyl radical production when photocatalytic experiments are designed using visible radiation within the wavelength region between 400 and 480 nm.

Preprints (www.preprints.org) | NOT PEER-REVIEWED | Posted: 29 September 2018 doi:10.20944/preprints201809.0583.v1

Peer-reviewed version available at Catalysts 2018, 8, 625; doi:10.3390/catal8120625

2.4. Photocatalytic Degradation of Estriol under High and Low UV-irradiation

The E3 photocatalytic degradation curves are shown in Figures 12a and 12b using high and low UV-irradiation, respectively. Fe content was found influencing the E3 photocatalytic degradation rate for both high and low UV-irradiation. In both cases, E3 photocatalytic degradation followed a pseudo-first-order model and the rate constant, k_1 (table 4), was obtained by fitting experimental data to $\ln([E3]/[E3_0])=k_1 t$.

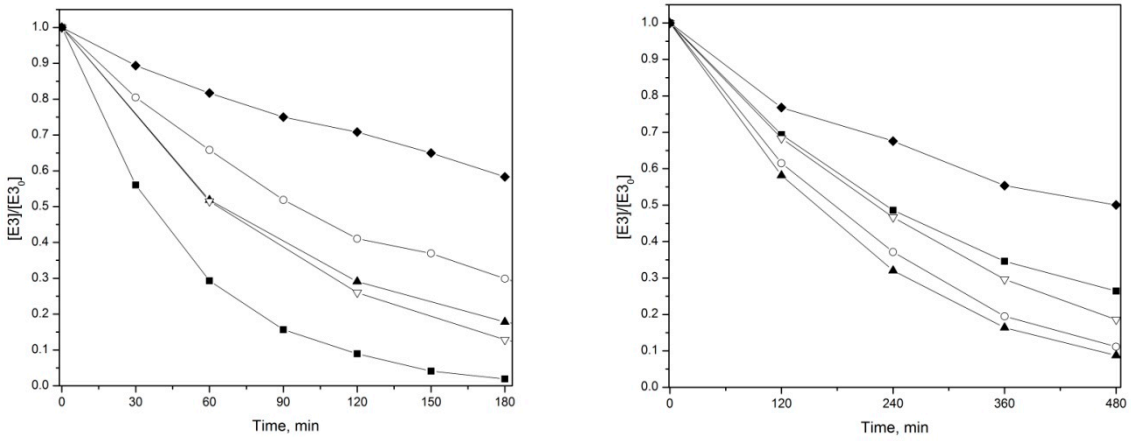

Figure 12. Photocatalytic degradation of E3 under high UV irradiation (a), and low UV irradiation (b); where ■ Aeroxide® TiO_2 P25, ○ zero-iron TiO_2, ▲ 0.3 Fe-TiO_2 TiO_2, ▽0.6 Fe-TiO_2, and ◆ 1.0 Fe-TiO_2 at pH 6 ± 0.1, and 20 °C.

Table 4. Kinetic values of E3 degradation using zero-iron TiO_2 and Fe-TiO_2.

Catalyst	Load	High UV-irradiation			Low UV-irradiation		
		k_1	R^2	$r_{0,E3}$	k_1	R^2	$r_{0,E3}$
	mg L^{-1}	min^{-1}		μM_{E3} min^{-1}	min^{-1}		μM_{E3} min^{-1}
TiO_2 Aeroxide® P25	20	0.021	0.996	0.21	0.003	0.992	0.030
Zero-iron TiO_2	320	0.007	0.997	0.069	0.004	0.991	0.040
0.3 Fe-TiO_2	320	0.009	0.994	0.090	0.005	0.992	0.042
0.6 Fe-TiO_2	320	0.011	0.997	0.099	0.003	0.999	0.030
1.0 Fe-TiO_2	320	0.003	0.979	0.027	0.001	0.987	0.012

Figure 13 shows pseudo-first order rate constant (k_1) of E3 photocatalytic degradation. In general, the photocatalytic activity first increased and then decreased as the Fe concentration increases similar to the behavior of previous studies with others organic molecules [22,26,62].

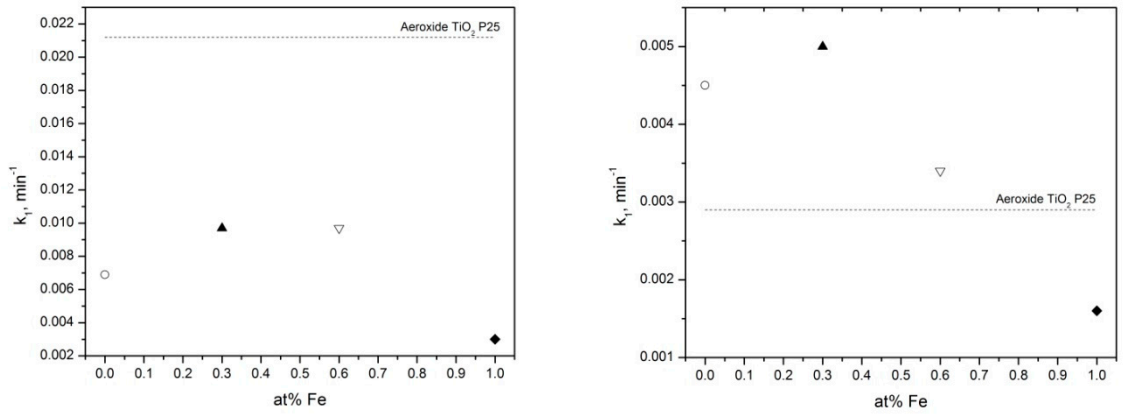

Preprints (www.preprints.org) | NOT PEER-REVIEWED | Posted: 29 September 2018 doi:10.20944/preprints201809.0583.v1

Peer-reviewed version available at Catalysts 2018, 8, 625; doi:10.3390/catal8120625

Figure 13. Photocatalytic reaction rate (k_1) for degradation of E3 under high UV irradiation(a), and low UV irradiation b) at pH 6 ± 0.1, and 20 °C.

Under high UV irradiation (Figure 13a), 0.6 Fe-TiO_2 k_1 was higher than for zero-iron TiO_2, 0.3 Fe-TiO_2 and 0.6 Fe-TiO_2. The increase of photocatalytic performance of 0.6 Fe-TiO_2 could be related with the increase of lifetime of electron-hole pairs, since Fe created additional energy levels near the conduction band of TiO_2 as mechanism suggested in Figure 11.

Under low UV-irradiation (Figure 13b), zero-iron TiO_2, 0.3 Fe-TiO_2, and 0.6 Fe-TiO_2 showed more photocatalytic activity than Aeroxide® TiO_2 P25 probably because of Fe doping, co-dopants no intentionally added, particle size, and superficial area. Furthermore, 0.3 Fe-TiO_2 enhanced photocatalytic activity with k_1 value as high as 0.005 min^{-1}. The high photocatalytic activity of 0.3 Fe-TiO_2 was due to the synergistic effect of dopant and Fe content increased time life of e^- photogenerated and increasing efficiency of electron transfer. Co-doping of Fe-TiO_2 demonstrated synergistic effect to increase photocatalytic activity under visible light for 2% S co-doped [63], N co-doped [41], and $Fe_xTi_{1-x}O_{2-y}N_y$ [64]. Also, superficial property such as particle size of 6.9 nm and superficial area of 77.6 m2 g-1 contributed to facilitate the mass transfer between interface and E3 and sub-products. Efficiency resource was also achieved so 0.3 Fe-TiO_2 absorbance 8.21 % of emission spectra of the lamp below equivalent E_g wavelength over 0.8 % or 7.64 % of Aeroxide® TiO_2 P25 and zero-iron TiO_2 respectively.

Correlation between •OH generation and E3 degradation was obtained for 1) sorting •OH generation initial velocity ($r_{0,OH}$) of pair $r_{0,OH}$ and E3 degradation initial velocity ($r_{0,E3}$) and 2) fitting data to linear regression. Under high UV irradiation, the linear correlation was $r_{0,E3}$ = 0.091 $r_{0,OH}$ + 0.040 with R^2 equal to 0.465. Under low UV-irradiation the linear correlation was

$$r_{0,E3} = 0.66\, r_{0,OH} + 0.012 \quad (12)$$

with R^2 equal to 0.983. The correlation between the pair ($r_{0,OH}$, $r_{0,E3}$) under high UV irradiation was low to consider a linear relationship, as not only •OH caused but also holes (h^+) or reactive oxygen species could cause E3 degradation. However, a linear relationship irradiation was found between the pair ($r_{0,OH}$, $r_{0,E3}$) under low UV irradiation. The high correlation between •OH generation and E3 degradation was attributable to that •OH was the main reactive oxygen species, and h^+ had lower oxidation power because of reduction of the E_g–This suggestion supports the mechanisms proposed in figure 11 and the Fe into the lattice of TiO_2 reduced the E_g with a consistent reduction of redox potential mention by others [25].

The efficiency resource of the system Fe-TiO_2/Low-UV was obtained by the dimensional analysis of slope of Eq. 12. The units of slope are E3 moles degraded per •OH mol generated at initial time, so 0.66 E3 molecules underwent a degradation when one •OH was generated for the photocatalytic system independent of Fe doping content in TiO_2.

Hence the main mechanism of degradation of E3 under low UV irradiation was via electronic transfer of e^- to give rise •OH. Also, the enhanced photocatalytic activity of 0.3 Fe-TiO_2 under low UV-irradiation add evidence that trapping – recombination mechanism of Fe-TiO_2 can be controlled by irradiation intensity. So, we suggest there is a trade-off between the intensity of irradiation, trapping – recombination rate and •OH radicals produced, that worth further for better understanding.

2.5. Relationship between Fe Content and Kinetic Constant

According to Bloth´s theoretical model, the photonic efficiency increases linearly with the doping ratio due to the formation of the charge carrier trapping centers, while it concurrently decreases quadratically with the doping ratio due to the creation of recombination centers [65]. Alternatively, we suggest an empirical relationship between the E3 degradation pseudo-first order rate constant (k_1) and Fe content (at.%) in TiO_2 as described in Eq. (13).

$$k_1(\delta) = c\left[e^{-k_e(\delta+\alpha)} - e^{-k_a(\delta+\alpha)}\right] \quad (13)$$

Preprints (www.preprints.org) | NOT PEER-REVIEWED | Posted: 29 September 2018 doi:10.20944/preprints201809.0583.v1

Peer-reviewed version available at Catalysts 2018, 8, 625; doi:10.3390/catal8120625

Where k_1 pseudo-first order constant, k_e is electron trap constant, k_a electron recombination constant, δ at % doped TiO_2, and c and α system constant. To solve the model described in Eq. (13), a numerical approximation by root-mean-square error minimization method was used according to to Eq. (14).

$$\varepsilon = \sqrt{\frac{1}{n}\sum_{i}\left|\overline{[k_{1.i}]} - [k_{1.i}]\right|} \quad (14)$$

where $\overline{[k_{1.i}]}$ is the theoretical k_1 value, $[k_{1.i}]$ is the experimental k_1 value, n is the number of data, and ε is the root-mean-square error. The solution of Eq. (14) was performed by simultaneously solving k_e, k_a, c and α using Excel Solver®. As an example, photocatalytic degradation of E3 under low UV- irradiation lamp shown in Figure 13b was fitted to Eq. (13) as shown in Figure 14.

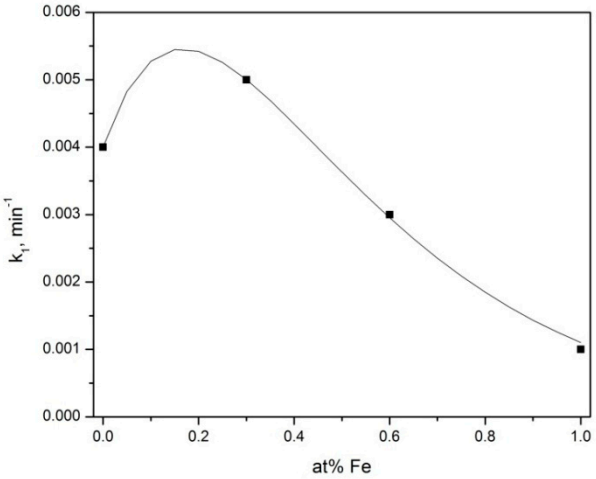

Figure 14. Experimental relationship between pseudo first order constant and at. % content.

The empirical model solved is in Eq. (15) and show that electron trap constant (k_e) overcome electron recombination (k_a) before optimal catalyst load. This model could lead to experimental work doping TiO_2 to the region where the optimal content of Fe gives rise maximum E3 degradation.

$$k_1(\delta) = -1.16\left[e^{-3.56(\delta+0.12)} - e^{-3.52(\delta+0.12)}\right] \quad (15)$$

3. Materials and Methods

3.1. Reagents

Sigma-Aldrich supplied estriol (E3, $C_{18}H_{24}O_3$, ≥ 97 %), titanium isopropoxide (TTIP, $Ti[OCH(CH_3)_2]_4$, 97 %), N,N-Dimethyl-4-nitrosoaniline (pNDA, also called RNO, $C_8H_{10}N_{20}$, 97 %), Sodium Dodecyl Sulfate (SDS), iron(III) nitrate ($Fe(NO_3)_3 \bullet 9H_2O$, > 99.99 %). Aeroxide® TiO_2 P25 (formerly Degussa P25 with 50 ± 15 m^2 g^{-1} of the specific surface area, 21 nm of average particle size, 80: 20 of anatase: rutile ratio according to the manufacturer) granted by Evonik Industries was the photocatalytic standard. Fremont supplied HNO_3, H_2SO_4, absolute ethanol, HPLC grade methanol, and HPLC grade water. All chemicals were used as received.

3.2. Photoreactor Setup

Figure 15 depicts the photoreactor which was a cylindrical water-jacketed glass vessel (318 mL) with 102 mm and 63 mm of interior height and diameter respectively. The horizontal and vertical position of the photoreactor was constant for all experiments. Lamps were horizontally set and centered to the photoreactor overhead. Two 15 W GE F15T8 BLB lamps (also called black-light lamp) supplied high UV-irradiation, and two 15 W GE F15T8 D lamps (also called daylight lamp) provided

Preprints (www.preprints.org) | NOT PEER-REVIEWED | Posted: 29 September 2018 doi:10.20944/preprints201809.0583.v1

Peer-reviewed version available at Catalysts 2018, 8, 625; doi:10.3390/catal8120625

low UV-irradiation. The overall system was in a closed box to avoid the effects of sunlight or any artificial radiation source. Lamp emission spectra were measured using a lab-made spectrophotometer with a webcam CMOS, with a diffraction grating of 1000 lines mm^{-1}, and without UV optical filter [66,67]. Emission spectra calibration of spectrophotometer was developed using 9 W fluorescent lamp (Tecnolite). The temperature of all experiments was set at 20 °C with a thermostatic bath with recirculation (Polystat, Cole-Palmer). An optical filter was not used in experiments, so visible light condition was not simulated.

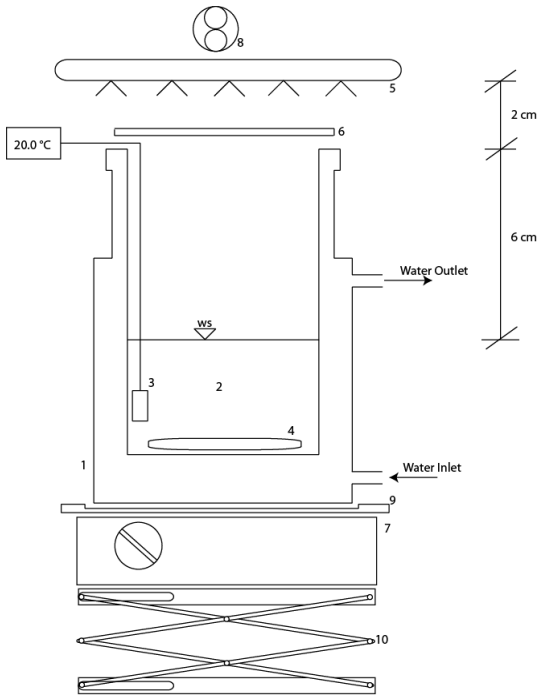

Figure 15. Scheme of photoreactor used for experiments: glass reactor (1), testing solution (2), temperature probe (3), spin bar (4), lamps (5), an optical filter (if needed) (6), stirring plate (7), cooling fan (8), horizontal position template (9), and lab jack lifting platform (10).

3.3. Synthesis of Materials

The method synthesis of iron-doped TiO_2 (Fe-TiO_2) materials followed the hydrothermal sol-gel synthetic approach proposed by Patra *et al.* with some differences precursor and thermal treatment [46]. First, a solution A was prepared to dissolve 1.44 g of SDS in 10 mL of deionized water. Then, four different solutions B were prepared to dissolve iron (III) nitrate in 2 mL of absolute ethanol (≥99.8 %) and slowly to add 3 mL of TTIP. The amounts of iron (III) nitrate were 0, 0.4, 4.3, and 42.6 mg of $Fe(NO_3)_3 \bullet 9H_2O$ identified as zero-iron TiO_2, 0.3 Fe-TiO_2, 0.6 Fe-TiO_2, and 1.0 Fe-TiO_2 respectively. Once ready, solution A was continuously stirred, and solution B was slowly dropped to solution A. The resulting mixture was adjusted to pH equal to 1 using concentrated HNO_3 and stirred for 3 h. The mixture was kept at 3 °C for 36 h. The solid precipitated was collected by filtration using Whatman Quantitative Filter Paper Grade 42. The materials were simultaneously dried, and calcinated with programmed thermal treatment (Isotemp® Programmable Muffle Furnace, Fisher Scientific) as following first the temperature increased from ambient temperature to 353 K with temperature ramp of 1 K min^{-1}, and hold for 720 min; then the temperature increased from 353 K to 773 K with a temperature ramp of 1 K min^{-1}, and keep for 360 min; and finally the temperature decreased from 773 K to 353 K with a temperature ramp of -1 K min^{-1}, and turned off the furnace. The materials were washed with 50:50 methanol-water and dried to 377 K overnight.

3.4. Materials Characterization

X-ray photoelectron spectroscopy (XPS) was performed using a Thermo Scientific K-Alpha X-ray photoelectron spectrometer with a monochromatized Al Kα X-ray source (1,487 V).

Preprints (www.preprints.org) | NOT PEER-REVIEWED | Posted: 29 September 2018 doi:10.20944/preprints201809.0583.v1

Peer-reviewed version available at Catalysts 2018, 8, 625; doi:10.3390/catal8120625

UV-Visible reflectance spectroscopy was obtained with Video Barrelino integrating sphere coupled to Carry 50 Conc Spectrophotometer. Diffuse reflectance spectra were transformed using the Kubelka-Monk method to obtain E_g of zero-iron TiO_2 and Fe-TiO_2 materials. Kubelka-Monk method plots $(F(R)hv)^{1/2}$ versus hv, draws a tangent at the inflection point on the curve and estimates E_g with hv value at the intersection with abscissa. In this case, $F(R)$ is a reflectance function equal to $(1-R)^2/2R$, R is the reflectance percentage, h is the Planck's constant, and v is frequency.

XRD patterns were recorded in a Siemens D-5000 Diffractometer using Cu K_α radiation (λ= 1.54060 Å) from 10° to 85°. The procedure for phases identification was using the QualX2 software with database developed by Altomare *et al.* [68]. The cards used for identification were 00-901-5929, 00-900-1681, and 00-900-4140 for anatase, rutile, and brookite, respectively. The quantification phases followed the method proposed by Spurr and Myers according to Eq 16.

$$f = \frac{1}{1 + 1.26\frac{I_R}{I_A}} \quad (16)$$

where f is the anatase percentage, I_A is intensity at a diffraction angle 2θ of 25.36°, and I_R is intensity at a diffraction angle 2θ of 27.46° [69].

The particle size was estimated by Scherer´s formula described in Eq. (17), where β is the full width at half maximum of the diffraction peaks (radians), k is the shape constant, λ is the wavelength of the incident Cu K_α radiation (λ= 1.54060 Å), θ is the Bragg's angle (radians), and D is the particle size (Å).

$$D = \frac{k\,\lambda}{\beta\,cos\theta} \quad (17)$$

Brunauer–Emmett–Teller (BET) isotherms were obtained in Nova Station A equipment. The surface morphology was observed by SEM in a JEOL ultrahigh resolution field emission electron microscope JSM-7800 F with 20 kV accelerating voltage, and 3 mm WD. Transmission electron microscopy (TEM) images were obtained in a JEM-2100 LaB6 electron microscope.

3.5. Hydroxyl Radical Generation

In this work pNDA bleaching was selected as a probe of •OH since pNDA was useful for measuring the photocatalytic performance of TiO_2 [48,57,70] with some advantages: 1) it is selective of the reaction of pNDA with •OH [71], 2) the high reaction rate with •OH on the order of 10^{10} M^{-1} s^{-1} [48,72], 3) easy application by observing bleaching at 440 nm following Beer´s Law, and bleaching of pNDA ran yellowish solution to transparent solution and 4) 1:1 stoichiometry, meaning that one •OH can bleach one pNDA molecule [48,56,58,59].

pNDA Absorption measurements were obtained using a UV-Visible spectrophotometer (Hatch DR/4000U). at 440 nm because of strong absorption as shown in Figure 16 and following Lamber-Beer law. pNDA test solution was 10 μM initial concentration and pH 6.0 ± 0.1 adjusted using NaOH or HCl when needed. No buffer solutions were used because them competes for •OH. Final pH was verified at the end of tests to discharge pH-pNDA bleaching.

Preprints (www.preprints.org) | NOT PEER-REVIEWED | Posted: 29 September 2018 doi:10.20944/preprints201809.0583.v1

Peer-reviewed version available at Catalysts 2018, 8, 625; doi:10.3390/catal8120625

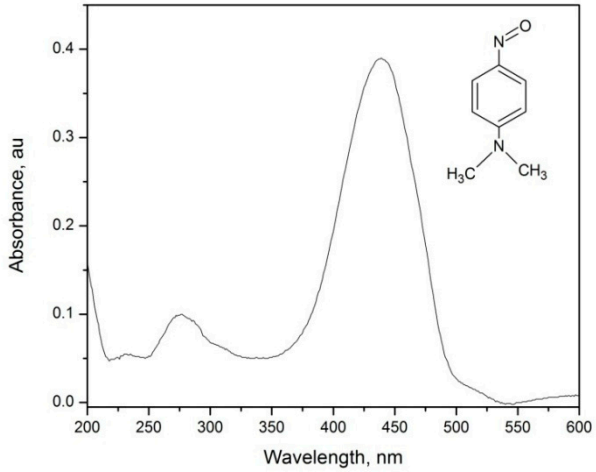

Figure 16. Structural formula and absorbance spectrum of pNDA.

The photocatalytic standard was Aeroxide® TiO_2 P25, and the load was 20 mg L^{-1}. Authors chose that catalyst load because of the previous study on efficiency resource [13]. The catalyst loading used for zero-iron TiO_2 and Fe-TiO_2 materials was 320 mg L^{-1}. Different catalyst load was used to set a baseline of •OH generation rates under high UV-irradiation. Catalyst load differences were attributable to aggregation of lab-made TiO_2.

The photocatalytic experiments were as next mentioned. First, a pNDA test solution was set at 20°C, the catalyst was added, and the suspension was mixed for 20 minutes without radiation. To evaluate the absorption of pNDA on TiO_2, an aliquot was withdrawn and centrifuged. Then, the system was fully illuminated, and aliquots were withdrawn after specific periods. Each of the samples was centrifuged at 6000 rpm for 15 minutes (Biofuge Primo, Sorvall) and measured in the UV-Visible spectrophotometer.

3.6. Photolysis and Photocatalytic Degradation of E3

The initial E3 concentration was 10 µM because 1) this research was part of a project focused on removal of E3 in water using sequentially coupled membrane filtration, 2) solubility limit of E3 in water was previously reported being 11.1 µM [73], and 45.1 µM [8,74], and 3) sensitivity of the analytical techniques used in this work. The E3 solution was prepared to dissolve 2.88 mg of E3 in 1 L of deionized water by stirring at room conditions in the dark for six hours. Working solutions were stored in an amber flask.

Each photocatalytic experiment used 100 mL of E3 working solution. Initial pH was adjusted to obtain a similar surface charge of TiO_2 [75]. Depending on the initial water conditions, the initial pH value was adjusted to 6.0 ± 0.1 using NaOH or HCl when needed. A dark period (no radiation) was allowed for 20 min. Then, similar experimental conditions were carried out as described in section 2.5. Additionally, the aliquots withdrawn from suspension were filtered using a 0.1 µm syringe filter (MillexVV, Millipore). The blank experiment without irradiation and TiO_2 photocatalyst was conducted for comparison. The blank experiment shows that de E3 cannot be degraded in absences of either TiO_2 or UV light.

3.7. Analytical Methods

The E3 concentration was monitored using an HPLC system (Waters 1515) equipped with a UV detector (Waters 2787) and an injection volume of 20 µL. The analytical method was performed in isocratic analytical mode using an Inertsil® ODS-3 column (150 mm × 4.6 mm, 5 µm) thermostated at 25 °C. The wavelength was at 280 nm according to E3 maximum absorbance. The mobile phase was

Preprints (www.preprints.org) | NOT PEER-REVIEWED | Posted: 29 September 2018 doi:10.20944/preprints201809.0583.v1

Peer-reviewed version available at Catalysts 2018, 8, 625; doi:10.3390/catal8120625

methanol (49%), and deionized water (51%) at a flow rate of 1 mL min^{-1}. The retention time of E3 was 10 minutes, and the limit of E3 detection was 0.1 μM (0.029 mg L^{-1}).

4. Conclusions

This work about Fe-TiO_2 give an understanding about the relationship between Fe doping ratio and intensity radiation for •OH generation and estriol (E3) degradation where main results are that: E3 degradation using 0.3 Fe-TiO_2 was feasible and can be improved with control irradiation intensity as a trade-off light absorption and catalytic reaction rate; the synthesis method and thermal treatment allowed nanoparticles with large superficial areas, and iron ions into the lattice of TiO_2; trapping recombination centers changing could be controlled with irradiation intensity to enhance the photocatalytic activity.

Thus, our present findings open the opportunity to reconsider before works where Fe doped TiO_2 impaired photocatalytic activity, and to advance on an application where irradiation should be controlled. For example, Fe-TiO2 can potentially be applied to medical use where low irradiation intensity should be applied to avoid adverse effects in humans or wildlife as also suggested by others [76].

Acknowledgments: The research was partially supported by CONACYT under Project CB-2011/168285. The Aeroxide® P25 Evonik catalyst used for this work was provided by Intertrade S.A. de C.V., the supplier of Evonik Industries in Mexico. The authors thank Ph.D. L. Lartundo-Rojas, Ph.D. Raul Borja Urbi, Ph.D. Hugo Martinez Gutiérrez, and Bio. Joao Jairzinho Salinas Camargo, for his assistance in XPS spectroscopy, TEM images, SEM images, and absorption isotherms respectively all of them from Centro de Nanociencias y Micro y Nanotecnología (CNMN) of IPN, Mexico. The authors thank Dr. M.A. Quiroz Alfaro for his excellent technical helping and had allowed using of materials and equipment at the UDLAP's electrochemical lab.

Author Contributions: Funding acquisition, Erick R. Bandala; Investigation, Irwing M. Ramírez-Sánchez; Project administration, Erick R. Bandala; Supervision, Erick R. Bandala; Writing – original draft, Irwing M. Ramírez-Sánchez; Writing – review & editing, Erick R. Bandala.

Conflicts of Interest: The authors declare no conflict of interest.

References

1. Dulio, V.; van Bavel, B.; Brorström-Lundén, E.; Harmsen, J.; Hollender, J.; Schlabach, M.; Slobodnik, J.; Thomas, K.; Koschorreck, J. Emerging pollutants in the EU: 10 years of NORMAN in support of environmental policies and regulations. *Environ. Sci. Eur.* **2018**, *30*.
2. Mandaric, L.; Celic, M.; Marcé, R.; Petrovic, M. Introduction on Emerging Contaminants in Rivers and Their Environmental Risk. In *Emerging Contaminants in River Ecosystems: Occurrence and Effects Under Multiple Stress Conditions*; Petrovic, M.; Sabater, S.; Elosegi, A.; Barceló, D., Eds.; Springer International Publishing: Cham, **2016**; pp. 3–25.
3. Houtman, C. J.; Legler, J.; Thomas, K. Effect-Directed Analysis of Complex Environmental Contamination. In; Brack, W., Ed.; Springer Berlin Heidelberg: Berlin, Heidelberg, **2011**; pp. 237–265.
4. Dimogerontas, G.; Liapi, C. Endocrine Disruptors (Xenoestrogens): An Overview. In *Plastics in Dentistry and Estrogenicity: A Guide to Safe Practice*; Eliades, T.; Eliades, G., Eds.; Springer Berlin Heidelberg: Berlin, Heidelberg, **2014**; pp. 3–48.
5. Hileman, B. Environmental Estrogens linked to Reproductive Abnormalities, Cancer. *Chem. Eng. News Arch.* **1994**, *72*, 19–23.
6. Prat, N.; Rieradevall, M.; Barata, C.; Munné, A. The combined use of metrics of biological quality and biomarkers to detect the effects of reclaimed water on macroinvertebrate assemblages in the lower part of a polluted Mediterranean river (Llobregat River, {NE} Spain). *Ecol. Indic.* **2013**, *24*, 167–176.
7. Souza, M. S.; Hallgren, P.; Balseiro, E.; Hansson, L. A. Low concentrations, potential ecological consequences: Synthetic estrogens alter life-history and demographic structures of aquatic invertebrates. *Environ. Pollut.* **2013**, *178*, 237–243.
8. Silva, C. P.; Otero, M.; Esteves, V. Processes for the elimination of estrogenic steroid hormones from water: A review. In *Environmental Pollution*; **2012**; Vol. 165, pp. 38–58.

Preprints (www.preprints.org) | NOT PEER-REVIEWED | Posted: 29 September 2018 doi:10.20944/preprints201809.0583.v1

Peer-reviewed version available at Catalysts 2018, 8, 625; doi:10.3390/catal8120625

9. Rodriguez-Narvaez, O. M.; Peralta-Hernandez, J. M.; Goonetilleke, A.; Bandala, E. R. Treatment technologies for emerging contaminants in water: A review. *Chem. Eng. J.* **2017**, *323*, 361–380.
10. Ramirez-Sanchez, I. M.; Mendez-Rojas, M. A.; Bandala, E. R. CHAPTER 25 Photocatalytic Degradation of Natural and Synthetic Estrogens with Semiconducting Nanoparticles. In *Advanced Environmental Analysis: Applications of Nanomaterials{,} Volume 2*; The Royal Society of Chemistry, **2017**; Vol. 2, pp. 153–177.
11. Ohko, Y.; Iuchi, K.; Niwa, C.; Tatsuma, T.; Nakashima, T.; Iguchi, T.; Kubota, Y.; Fujishima, A. 17β-Estradiol Degradation by TiO2 Photocatalysis as a Means of Reducing Estrogenic Activity. *Environ. Sci. Technol.* **2002**, *36*, 4175–4181.
12. Coleman, H. M.; Routledge, E. J.; Sumpter, J. P.; Eggins, B. R.; Byrne, J. A. Rapid loss of estrogenicity of steroid estrogens by UVA photolysis and photocatalysis over an immobilised titanium dioxide catalyst. *Water Res.* **2004**, *38*, 3233–3240.
13. Ramírez-Sánchez, I. M.; Tuberty, S.; Hambourger, M.; Bandala, E. R. Resource efficiency analysis for photocatalytic degradation and mineralization of estriol using TiO2 nanoparticles. *Chemosphere* **2017**, *184*, 1270–1285.
14. Hashimoto, K.; Irie, H.; Fujishima, A. Photocatalysis: A Historical Overview and Future Prospects. *Jpn. J. Appl. Phys.* **2005**, *44*, 8269–8285.
15. Fujishima, A.; Zhang, X.; Tryk, D. A. TiO2 photocatalysis and related surface phenomena. *Surf. Sci. Rep.* **2008**, *63*, 515–582.
16. Tong, A. Y. C.; Braund, R.; Warren, D. S.; Peake, B. M. TiO2-assisted photodegradation of pharmaceuticals - A review. *Cent. Eur. J. Chem.* **2012**, *10*, 989–1027.
17. Cassaignon, S.; Colbeau-Justin, C.; Durupthy, O. Titanium dioxide in photocatalysis. In *Nanomaterials: A Danger or a Promise?: A Chemical and Biological Perspective*; **2013**; pp. 153–188.
18. Augugliaro, V.; Loddo, V.; Pagliaro, M.; Palmisano, G.; Palmisano, L. *Clean by Light Irradiation: Practical Applications of Supported TiO2*; RSC Publishing: Cambridge, UK, **2010**.
19. Etacheri, V.; Di Valentin, C.; Schneider, J.; Bahnemann, D.; Pillai, S. C. Visible-light activation of TiO2 photocatalysts: Advances in theory and experiments. *J. Photochem. Photobiol. C Photochem. Rev.* **2015**, *25*, 1–29.
20. Yu, H.; Irie, H.; Hashimoto, K. Conduction band energy level control of titanium dioxide: Toward an efficient visible-light-sensitive photocatalyst. *J. Am. Chem. Soc.* **2010**, *132*, 6898–6899.
21. Choi, W.; Termin, A.; Hoffmann, M. R. The role of metal ion dopants in quantum-sized TiO2: Correlation between photoreactivity and charge carrier recombination dynamics. *J. Phys. Chem.* **1994**, *98*, 13669–13679.
22. Wen, L.; Liu, B.; Zhao, X.; Nakata, K.; Murakami, T.; Fujishima, A. Synthesis, Characterization, and Photocatalysis of Fe-Doped TiO2: A Combined Experimental and Theoretical Study. *Int. J. Photoenergy* **2012**, 1–10.
23. Kaur, T.; Sraw, A.; Wanchoo, R. K.; Toor, A. P. Visible –Light Induced Photocatalytic Degradation of Fungicide with Fe and Si Doped TiO2 Nanoparticles. *Mater. Today Proc.* **2016**, *3*, 354–361.
24. Zhao, B.; Mele, G.; Pio, I.; Li, J.; Palmisano, L.; Vasapollo, G. Degradation of 4-nitrophenol (4-NP) using Fe-TiO2 as a heterogeneous photo-Fenton catalyst. *J. Hazard. Mater.* **2010**, *176*, 569–574.
25. Yalçın, Y.; Kılıç, M.; Çınar, Z. Fe+3-doped TiO2: A combined experimental and computational approach to the evaluation of visible light activity. *Appl. Catal. B Environ.* **2010**, *99*, 469–477.
26. Cai, L.; Liao, X.; Shi, B. Using Collagen Fiber as a Template to Synthesize TiO2 and Fex/TiO2 Nanofibers and Their Catalytic Behaviors on the Visible Light-Assisted Degradation of Orange II. *Ind. Eng. Chem. Res.* **2010**, *49*, 3194–3199.
27. Li, J.; Xu, J.; Dai, W. L.; Li, H.; Fan, K. Direct hydro-alcohol thermal synthesis of special core-shell structured Fe-doped titania microspheres with extended visible light response and enhanced photoactivity. *Appl. Catal. B Environ.* **2009**, *85*, 162–170.
28. Tong, T.; Zhang, J.; Tian, B.; Chen, F.; He, D. Preparation of Fe3+-doped TiO2catalysts by controlled hydrolysis of titanium alkoxide and study on their photocatalytic activity for methyl orange degradation. *J. Hazard. Mater.* **2008**, *155*, 572–579.
29. Ambrus, Z.; Bal??zs, N.; Alapi, T.; Wittmann, G.; Sipos, P.; Dombi, A.; Mogyor??si, K. Synthesis, structure and photocatalytic properties of Fe(III)-doped TiO2 prepared from TiCl3. *Appl. Catal. B Environ.* **2008**, *81*, 27–37.
30. Cong, Y.; Zhang, J.; Chen, F.; Anpo, M.; He, D. Preparation, photocatalytic activity, and mechanism of nano-TiO2 Co-doped with nitrogen and iron (III). *J. Phys. Chem. C* **2007**, *111*, 10618–10623.

Preprints (www.preprints.org) | NOT PEER-REVIEWED | Posted: 29 September 2018 doi:10.20944/preprints201809.0583.v1

Peer-reviewed version available at Catalysts 2018, 8, 625; doi:10.3390/catal8120625

31. Adán, C.; Bahamonde, A.; Fernández-García, M.; Martínez-Arias, A. Structure and activity of nanosized iron-doped anatase TiO2catalysts for phenol photocatalytic degradation. *Appl. Catal. B Environ.* **2007**, *72*, 11–17.
32. Yamashita, H.; Harada, M.; Misaka, J.; Takeuchi, M.; Neppolian, B.; Anpo, M. Photocatalytic degradation of organic compounds diluted in water using visible light-responsive metal ion-implanted TiO2catalysts: Fe ion-implanted TiO2. In *Catalysis Today*; **2003;** Vol. 84, pp. 191–196.
33. Li, X.; Yue, P.-L.; Kutal, C. Synthesis and photocatalytic oxidation properties of iron doped titanium dioxide nanosemiconductor particles. *New J. Chem.* **2003**, *27*, 1264.
34. Zhang, Z.; Wang, C.-C.; Zakaria, R.; Ying, J. Y. Role of Particle Size in Nanocrystalline TiO2-Based Photocatalysts. *J. Phys. Chem. B* **1998**, *102*, 10871–10878.
35. Litter, M. I.; Navío, J. A. Photocatalytic properties of iron-doped titania semiconductors. *J. Photochem. Photobiol. A Chem.* **1996**, *98*, 171–181.
36. Fàbrega, C.; Andreu, T.; Cabot, A.; Morante, J. R. Location and catalytic role of iron species in TiO2:Fe photocatalysts: An EPR study. *J. Photochem. Photobiol. A Chem.* **2010**, *211*, 170–175.
37. Seabra, M. P.; Salvado, I. M. M.; Labrincha, J. A. Pure and (zinc or iron) doped titania powders prepared by sol-gel and used as photocatalyst. *Ceram. Int.* **2011**, *37*, 3317–3322.
38. Abazović, N. D.; Mirenghi, L.; Janković, I. A.; Bibić, N.; Šojić, D. V.; Abramović, B. F.; Čomor, M. I. Synthesis and characterization of rutile TiO 2 nanopowders doped with iron ions. *Nanoscale Res. Lett.* **2009**, *4*, 518–525.
39. Geissen, V.; Mol, H.; Klumpp, E.; Umlauf, G.; Nadal, M.; van der Ploeg, M.; van de Zee, S. E. A. T. M.; Ritsema, C. J. Emerging pollutants in the environment: A challenge for water resource management. *Int. Soil Water Conserv. Res.* **2015**, *3*, 57–65.
40. Lin, T. C.; Seshadri, G.; Kelber, J. A. A consistent method for quantitative XPS peak analysis of thin oxide films on clean polycrystalline iron surfaces. *Appl. Surf. Sci.* **1997**, *119*, 83–92.
41. Xing, M.; Wu, Y.; Zhang, J.; Chen, F. Effect of synergy on the visible light activity of B, N and Fe co-doped TiO2 for the degradation of MO. *Nanoscale* **2010**, *2*, 1233.
42. Lopez, R.; Gomez, R. Band-gap energy estimation from diffuse reflectance measurements on sol-gel and commercial TiO 2: A comparative study. *J. Sol-Gel Sci. Technol.* **2012**, *61*, 1–7.
43. Shi, J.; Chen, G.; Zeng, G.; Chen, A.; He, K.; Huang, Z.; Hu, L.; Zeng, J.; Wu, J.; Liu, W. Hydrothermal synthesis of graphene wrapped Fe-doped TiO2nanospheres with high photocatalysis performance. *Ceram. Int.* **2018**, *44*, 7473–7480.
44. Yu, J.; Xiang, Q.; Zhou, M. Preparation, characterization and visible-light-driven photocatalytic activity of Fe-doped titania nanorods and first-principles study for electronic structures. *Appl. Catal. B Environ.* **2009**, *90*, 595–602.
45. Goswami, P.; Ganguli, J. N. Evaluating the potential of a new titania precursor for the synthesis of mesoporous Fe-doped titania with enhanced photocatalytic activity. *Mater. Res. Bull.* **2012**, *47*, 2077–2084.
46. Patra, A. K.; Dutta, A.; Bhaumik, A. Highly ordered mesoporous TiO2-Fe2O3 mixed oxide synthesized by sol-gel pathway: an efficient and reusable heterogeneous catalyst for dehalogenation reaction. *ACS Appl. Mater. Interfaces* **2012**, *4*, 5022–8.
47. Luttrell, T.; Halpegamage, S.; Tao, J.; Kramer, A.; Sutter, E.; Batzill, M. Why is anatase a better photocatalyst than rutile? - Model studies on epitaxial TiO2 films. *Sci. Rep.* **2014**, *4*, 4043.
48. Zang, L.; Qu, P.; Zhao, J.; Shen, T.; Hidaka, H. Photocatalytic bleaching of p-nitrosodimethylaniline in TiO2 aqueous suspensions: A kinetic treatment involving some primary events photoinduced on the particle surface. *J. Mol. Catal. A Chem.* **1997**, *120*, 235–245.
49. Othman, S. H.; Abdul Rashid, S.; Mohd Ghazi, T. I.; Abdullah, N. Fe-Doped TiO2 Nanoparticles Produced via MOCVD: Synthesis, Characterization, and Photocatalytic Activity. *J. Nanomater.* 2011, *2011*, 1–8.
50. Teoh, W. Y.; Amal, R.; Mädler, L.; Pratsinis, S. E. Flame sprayed visible light-active Fe-TiO2 for photomineralisation of oxalic acid. *Catal. Today* **2007**, *120*, 203–213.
51. Pongwan, P.; Inceesungvorn, B.; Wetchakun, K.; Phanichphant, S.; Wetchakun, N. Highly efficient visible-light-induced photocatalytic activity of Fe-doped TiO 2 nanoparticles. *Eng. J.* **2012**, *16*, 143–151.
52. Kruk, M.; Jaroniec, M. Gas adsorption characterization of ordered organic-inorganic nanocomposite materials. *Chem. Mater.* **2001**, *13*, 3169–3183.
53. Limousin, G.; Gaudet, J. P.; Charlet, L.; Szenknect, S.; Barthès, V.; Krimissa, M. Sorption isotherms: A review on physical bases, modeling and measurement. *Appl. Geochemistry* **2007**, *22*, 249–275.

Preprints (www.preprints.org) | NOT PEER-REVIEWED | Posted: 29 September 2018 doi:10.20944/preprints201809.0583.v1

Peer-reviewed version available at Catalysts 2018, 8, 625; doi:10.3390/catal8120625

54. Choi, W.; Termin, A.; Hoffmann, M. R. The Role of Metal Ion Dopants in Quantum-Sized TiO2: Correlation between Photoreactivity and Charge Carrier Recombination Dynamics. *J. Phys. Chem.* **1994**, *98*, 13669–13679.
55. Serpone, N. Relative photonic efficiencies and quantum yields in heterogeneous photocatalysis. *J. Photochem. Photobiol. A Chem.* **1997**, *104*, 1–12.
56. Barashkov, N. N.; Eisenberg, D.; Eisenberg, S.; Shegebaeva, G. S.; Irgibaeva, I. S.; Barashkova, I. I. Electrochemical chlorine-free AC disinfection of water contaminated with Salmonella typhimurium bacteria. *Russ. J. Electrochem.* **2010**, *46*, 306–311.
57. Kim, C.; Park, H. J.; Cha, S.; Yoon, J. Facile detection of photogenerated reactive oxygen species in TiO2 nanoparticles suspension using colorimetric probe-assisted spectrometric method. *Chemosphere* **2013**, *93*, 2011–2015.
58. Martínez-Huitle, C. A.; Quiroz, M. A.; Comninellis, C.; Ferro, S.; De Battisti, A. Electrochemical incineration of chloranilic acid using Ti/IrO2, Pb/PbO2 and Si/BDD electrodes. *Electrochim. Acta* **2004**, *50*, 949–956.
59. Bors, W.; Michel, C.; Saran, M. On the nature of biochemically generated hydroxyl radicals. Studies using the bleaching of p-nitrosodimethylaniline as a direct assay method. *Eur. J. Biochem.* **1979**, *95*, 621–627.
60. Muff, J.; Bennedsen, L. R.; Søgaard, E. G. Study of electrochemical bleaching of p-nitrosodimethylaniline and its role as hydroxyl radical probe compound. *J. Appl. Electrochem.* **2011**, *41*, 599–607.
61. Zhu, J.; Zheng, W.; He, B.; Zhang, J.; Anpo, M. Characterization of Fe-TiO2photocatalysts synthesized by hydrothermal method and their photocatalytic reactivity for photodegradation of XRG dye diluted in water. *J. Mol. Catal. A Chem.* **2004**, *216*, 35–43.
62. Zhou, M.; Yu, J.; Cheng, B. Effects of Fe-doping on the photocatalytic activity of mesoporous TiO2 powders prepared by an ultrasonic method. *J. Hazard. Mater.* **2006**, *137*, 1838–1847.
63. Hamadanian, M.; Reisi-Vanani, A.; Behpour, M.; Esmaeily, A. S. Synthesis and characterization of Fe,S-codoped TiO2 nanoparticles: Application in degradation of organic water pollutants. *Desalination* **2011**, *281*, 319–324.
64. Naik, B.; Parida, K. M. Solar Light Active Photodegradation of Phenol over a FexTi1-xO2-yNy Nanophotocatalyst. *Ind. Eng. Chem. Res.* **2010**, *49*, 8339–8346.
65. Bloh, J. Z.; Dillert, R.; Bahnemann, D. W. Zinc Oxide Photocatalysis: Influence of Iron and Titanium Doping and Origin of the Optimal Doping Ratio. *ChemCatChem* **2013**, *5*, 774–778.
66. Lorenz, R. D. A simple webcam spectrograph. *Am. J. Phys.* **2014**, *82*, 169–173.
67. Widiatmoko, E.; Widayani; Budiman, M.; Abdullah, M.; Khairurrijal A simple spectrophotometer using common materials and a digital camera. *Phys. Educ.* **2011**, *46*, 332–339.
68. Altomare, A.; Corriero, N.; Cuocci, C.; Falcicchio, A.; Moliterni, A.; Rizzi, R. QUALX2.0 : a qualitative phase analysis software using the freely available database POW_COD. *J. Appl. Crystallogr.* **2015**, *48*, 598–603.
69. Spurr, R. a.; Myers, H. Quantitative Analysis of Anatase-Rutile Mixtures with an X-Ray Diffractometer. *Anal. Chem.* **1957**, *29*, 760–762.
70. Simonsen, M. E.; Muff, J.; Bennedsen, L. R.; Kowalski, K. P.; Søgaard, E. G. Photocatalytic bleaching of p-nitrosodimethylaniline and a comparison to the performance of other AOP technologies. *J. Photochem. Photobiol. A Chem.* **2010**, *216*, 244–249.
71. Kraljic, I.; Trumbore, C. N. p-Nitrosodimethylaniline as an OH radical scavenger in radiation chemistry. *J. Am. Chem. Soc.* **1965**, *87*, 2547–2550.
72. Farhataziz, A. B. R. *Selected specific rates of reactions of transients from water in aqueous solutions III: Hydroxyl radical and perhydroxyl radical and their radical ions*; Washington, 1977.
73. Hurwitz, A. R.; Liu, S. T. Determination of aqueous solubility and pKa values of estrogens. *J. Pharm. Sci.* **1977**, *66*, 624–627.
74. Ying, G. G.; Kookana, R. S.; Ru, Y. J. Occurrence and fate of hormone steroids in the environment. *Environ. Int.* 2002, *28*, 545–551.
75. Fernández-Ibáñez, P.; De Las Nieves, F. J.; Malato, S. Titanium Dioxide/Electrolyte Solution Interface: Electron Transfer Phenomena. *J. Colloid Interface Sci.* **2000**, *227*, 510–516.
76. George, S.; Pokhrel, S.; Ji, Z.; Henderson, B. L.; Xia, T.; Li, L.; Zink, J. I.; Nel, A. E.; Mädler, L. Role of Fe doping in tuning the band gap of TiO2 for the photo-oxidation-induced cytotoxicity paradigm. *J. Am. Chem. Soc.* **2011**, *133*, 11270–11278.